Three-Dimensional Mesoporous Graphene Aerogel-Supported SnO$_2$ Nanocrystals for High-Performance NO$_2$ Gas Sensing at Low Temperature

Lei Li,[†,‡] Shuijian He,[†,∥] Minmin Liu,[†,∥] Chunmei Zhang,[†,∥] and Wei Chen*[,†]

[†]State Key Laboratory of Electroanalytical Chemistry, Changchun Institute of Applied Chemistry, Chinese Academy of Sciences, Changchun 130022, People's Republic of China

[‡]The College of Electrical and Electronic Engineering, Changchun University of Technology, Changchun 130012, People's Republic of China

[∥]University of Chinese Academy of Sciences, Beijing 100039, People's Republic of China

S *Supporting Information*

ABSTRACT: A facile and cost-efficient hydrothermal and lyophilization two-step strategy has been developed to prepare three-dimensional (3D) SnO$_2$/rGO composites as NO$_2$ gas sensor. In the present study, two different metal salt precursors (Sn^{2+} and Sn^{4+}) were used to prepare the 3D porous composites. It was found that the products prepared from different tin salts exhibited different sensing performance for NO$_2$ detection. The scanning electron microscopy and transmission electron microscopy characterizations clearly show the macroporous 3D hybrids, nanoporous structure of reduce graphene oxide (rGO), and the supported SnO$_2$ nanocrystals with an average size of 2−7 nm. The specific surface area and porosity properties of the 3D mesoporous composites were analyzed by Braunauer−Emmett−Teller method. The results showed that the SnO$_2$/rGO composite synthesized from Sn^{4+} precursor (SnO$_2$/rGO-4) has large surface area (441.9 m^2/g), which is beneficial for its application as a gas sensing material. The gas sensing platform fabricated from the SnO$_2$/rGO-4 composite exhibited a good linearity for NO$_2$ detection, and the limit of detection was calculated to be as low as about 2 ppm at low temperature. The present work demonstrates that the 3D mesoporous SnO$_2$/rGO composites with extremely large surface area and stable nanostructure are excellent candidate materials for gas sensing.
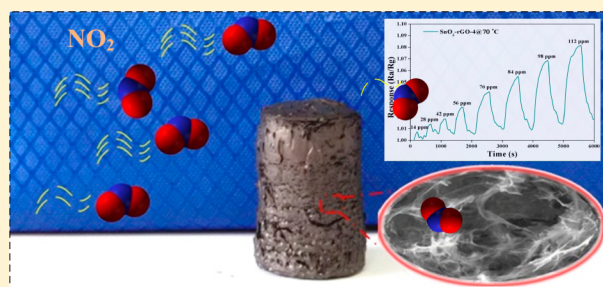
Tin oxide (SnO$_2$) is a typical n-type metal dioxide with rutile crystalline structure and a wide band gap of 3.6 eV at 300 K. Due to the excellent properties of SnO$_2$, such as high physical and chemical stability, nontoxicity, low cost, and so on, it has been widely used for various kinds of gas sensing applications such as ethanol,[1,2] nitric oxide,[3] formaldehyde,[4]etc. One of the characteristic gases sensing properties of SnO$_2$ is that its electrical conductivity varies with different types of target gases. In general, the electrical conductivity of this semiconductor material will increase when it is exposed in reducing gas, but decrease in oxidizing gas atmosphere. The rutile structure of SnO$_2$ possesses oxygen vacancies and interstitial atoms between the boundary of grains, and the defective structure will directly influence its gas sensing property. In other words, SnO$_2$ with more oxygen vacancies usually has higher sensitivity for gas sensing. Meanwhile, some significant disadvantages largely limit the application of SnO$_2$ semiconductor materials in gas sensors: (1) due to the wide band gap, the resistance of SnO$_2$ is relatively high at room temperature; (2) high operation temperature is usually necessary for the SnO$_2$-based gas sensors (for instance, 170−200 °C for H$_2$ sensing and above 200 °C for CO detection);

(3) in the synthesis process, the easy agglomeration will severely reduce the specific surface area and thus lower the sensing performance. Hence, to improve the sensing performances of semiconductor metal oxide-based sensors, these significant shortcomings have to be overcome first. In recent years, it was found that by depositing SnO$_2$ nanocrystals on a conductive and stable support, the electrical conductivity and dispersion can be effectively improved. Among the reported supports, carbon materials have been widely used, and they exhibited excellent stability and conductivity.

Graphene, a two-dimensional monolayer of sp^2-hybridized honeycomb-like carbon matrix, has very excellent performances in the electronic conductivity, specific surface area, porosity, thermal stability, and mechanical strength, etc. Typically, graphene, especially the chemically derived graphene, has been considered as a promising gas sensing material for gas detection at room temperature since their sensing properties were discovered by Schedin and Fowler et al.[5,6] Up to now,

various graphene-supported metal oxides have been developed for gas sensing.[7−9] During the procedure for the preparation of graphene-supported semiconductor nanocrystals, graphene acts as surfactant to avoid the agglomeration of metal oxide and also as oxidant to oxidize metal ions with low oxidation states. On the other hand, as an excellent conductive material, graphene support can enhance the electron transfer to target gas (or interior of composites) and improve the gas diffusion, especially for the 3D graphene aerogel with interconnected porous structure and high specific surface area. Actually, SnO_2/graphene nanocomposites have already demonstrated good electrochemical properties and promising applications in lithium-ion battery,[10−13] chemical sensing,[14−17,18,19] and so on. Among these applications, several SnO_2/graphene-based gas sensors have been reported by taking advantage of the high sensing performance.[20,21] Compared to unsupported SnO_2, the SnO_2/graphene composite has the following advantages. First, such hybrid composite overcomes the limit of high operation temperature of pure SnO_2 semiconductor material and can reduce the operation temperature to 50 °C, even as low as room temperature range.[20,22] Second, the graphene support can effectively prevent the aggregation of SnO_2 nanoparticles and reduce the size of SnO_2 grains.[13,23] Third, compared with pure SnO_2 semiconductor materials, the resistance of SnO_2/graphene can be reduced by several orders of magnitude.[15] However, previous work focused on simple graphene nanosheet-supported SnO_2 materials. To the best of our knowledge, there is no study on gas sensing performance of 3D graphene aerogel-supported SnO_2 hybrids, and there is no report on the influence of metal salt precursor (Sn^{2+}, Sn^{4+}) on the structure of product and the gas sensing properties.

In this work, we report a facile hydrothermal method to prepare 3D freestanding rGO-supported SnO_2 nanocomposites by using different metal salt precursors. Without any surfactant, SnO_2 nanoparticles are dispersed uniformly on the surface of 3D rGO aerogel through the present synthetic process. To study the potential application, gas sensing devices were fabricated from the as-synthesized SnO_2/rGO composites. It was found that the tin salt precursors have obvious effect on the morphology of the product and the gas sensing performance. The 3D SnO_2/rGO hybrid prepared from Sn^{4+} precursor exhibited outstanding sensing performance for NO_2 gas detection with high sensitivity, good linearity, and fast response. Moreover, with the present 3D SnO_2/rGO as sensing platform, the detection of NO_2 gas can be realized at low operation temperature.

■ EXPERIMENTAL SECTION

Materials Preparation. All reagents were analytical grade and were used without further purification unless that was specified. Graphene oxide (GO) was prepared by a modified Hummers method.[15] In a typical procedure, 1.4 g of preoxidized graphite powder was dissolved in 32.5 mL of concentrated H_2SO_4, and then 4.25 g of $KMnO_4$ was slowly added into the suspension, followed by magnetic stirring in ice bath condition for about 10 min. The suspension was transferred to oil bath environment still under vigorous stirring and was heated at 35 °C for another 2 h. Deionized water (160 mL) was then slowly added in the suspension until a homogeneous solution was obtained. Upon addition of 2 mL of H_2O_2 (30 wt %), the suspension was washed with 200 mL of diluent HCl (3 M) and filtered. After dialysis for about 1 week

and then centrifugation at 3000 rpm, the supernatant was collected for further use.

The preparation of the SnO_2/rGO composites was carried out as follows. Ten milliters of GO (3.6 mg/mL) suspension was sonicated for 30 min to form homogeneous solution. At the same time, 0.105 g of $SnCl_4·5H_2O$ and 0.054 g of urea were dissolved into 20 mL of deionized water under magnetic stirring for 10 min at room temperature (named Solution A). Then the prepared GO solution was dropwise added into Solution A under vigorous stirring for an hour. After that, the ropy colloid was transferred to a 50 mL Teflon-lined stainless steel vessel and heated at 180 °C for 16 h. After cooling down to room temperature, the three-dimensional (3D) SnO_2/rGO hydrogel was obtained, and after immersion in purified water several times, the obtained composite was further freeze-dried under −50 °C. Finally, the 3D freestanding mesoporous product of SnO_2/rGO aerogel was collected. Another different tin salt precursor, 0.066 g of $SnCl_2·2H_2O$, was also used to synthesize SnO_2/rGO following the same process described above. In order to distinguish these two composites, the products synthesized from $SnCl_4·5H_2O$ and $SnCl_2·2H_2O$ are denoted as SnO_2/rGO-4 and SnO_2/rGO-2, respectively. Pure rGO was also prepared for comparison.

Material Characterization. The crystal structures of the prepared samples were characterized by X-ray powder diffraction (XRD) on a Bruker D8 advance X-ray diffractometer (Cu−Kα, λ = 1.54 Å) from 10 to 90°. X-ray photoelectron spectroscopy (XPS) was performed on a VG Thermo ESCALAB 250 spectrometer (120 W, 100 eV). The morphology of the 3D hybrids was characterized by scanning electron microscopy (SEM), energy dispersive spectroscopy (EDS), transmission electron microscopy (TEM), and high-resolution TEM (HRTEM) on a XL30, JEOL 2000 transmission electron microscope and a JEM-2010(HR) microscope, respectively. Thermogravimetric analysis (TGA) was carried out on a Pyris Diamond TG/DTA system (operating temperature from 30 to 800 °C at 10 °C/min under air flow). Braunauer−Emmett−Teller (BET) specific surface area and porosity properties analysis were performed on the Quantachrome Autosorb Automated Gas Sorption System.

NO_2 Gas Sensing Test. First, the different synthesized sensing materials, including SnO_2/rGO-2, SnO_2/rGO-4, and rGO, were mixed with *N,N*-dimethylformamide (DMF) to make homogeneous suspensions. Gas sensing platforms were fabricated by dripping the suspensions on commercial ceramic substrates with Ag−Pd interdigitated electrodes. The prepared sensors were then dried at 60 °C for several hours in air. The gas sensing properties of the SnO_2/rGO hybrids were then characterized on a CGS-1TP (Chemical Gas Sensor-1 Temperature Pressure, Beijing Elite Tech Co., Ltd., China) intelligent gas sensing analysis system (Figure 1a). The resistance values of the gas sensors were acquired at different operating temperatures which were adjusted by heating the ceramic plate through the Thermo controller. The highest operating temperature could reach 500 °C with a temperature rise rate of 5 °C/s. The ceramic substrate covered with sensing materials was first pressed on the ceramic plate by two metal probes and then preheated at the target operating temperature about 10−30 min. When the resistance value of sensor reaches almost a steady level, the test chamber with 18 L in volume was closed, and then NO_2 gas was injected into the chamber through injection pore with an injector. At the same time, the mixing fans were turned on until the resistance of the sensor reached a
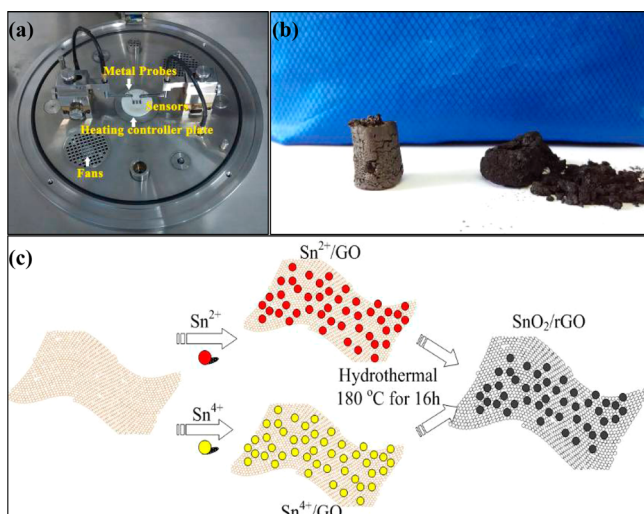
Figure 1. Photographs of (a) gas sensing system of CGS-1TP and (b) the 3D aerogel structures of SnO_2/rGO-4 (left) and SnO_2/rGO-2 (right) obtained after freeze-drying. (c) Schematic diagram of the formation of SnO_2/rGO nanocomposites from different tin salt precursors.

constant value. After measurements, the mixing gas fans were turned off and the test chamber was opened to make the sensor exposed in air. In this study, the response of a sensor was defined as the relative change of the resistance of the sensing material in air and in analyte: $R = R_a/R_g$, where R_a and R_g are the resistance values of a sensor in air and target gas, respectively. The concentration of NO_2 gas could be calculated by

$$Q = V \times C \times 10^{-6} \times \frac{273 + T_R}{273 + T_B} \tag{1}$$

where Q is the injected volume of NO_2, V is the volume of test chamber, C is the concentration of target gas (NO_2), and T_B and T_R are the testing and room temperatures, respectively.

■ RESULTS AND DISCUSSION

Characterization of the Samples. The obtained 3D structures and the overall preparation processes of the SnO_2/rGO-2 and SnO_2/rGO-4 composites through a hydrothermal reaction are displayed in Figure 1b and c. Obviously, for the SnO_2/rGO-4, a 3D column-like freestanding structure has been formed through the present synthetic route. However, the SnO_2/rGO-2 exhibits a fragile structure compared to the SnO_2/rGO-4. Note that both samples are composed of rutile SnO_2 supported on rGO, which can be derived from the following XRD measurements. Therefore, different tin salt precursors have effect on the morphology of the final products, which may be caused by the different formation processes. For the synthesis of rGO-supported SnO_2 from Sn^{2+}, the formation of SnO_2 nanocrystals and rGO may be produced from Sn(II) and GO, respectively, in the hydrothermal process. On the other hand, it is known that the standard reduction potential of Sn^{4+}/Sn^{2+} is relatively low (0.15 V), so the Sn^{2+}-contained precursor probably experienced a redox with GO solution and was readily oxidized from Sn^{2+} into Sn^{4+}. Such procedure also proves that the acidic GO solution has the oxidizing ability. However, the Sn^{4+}-contained precursor was first hydrolyzed to form [Sn-$(H_2O)_{6-x}(OH)_x]^{(4-x)+}$ and then reacted with functional groups on the surfaces and edges of graphene oxide sheets, such as hydroxyl, carboxyl, and epoxy, and subsequently dehydrated and crystallized into SnO_2 nanocrystals.[24,25] It should be pointed out that during these two reaction procedures, urea
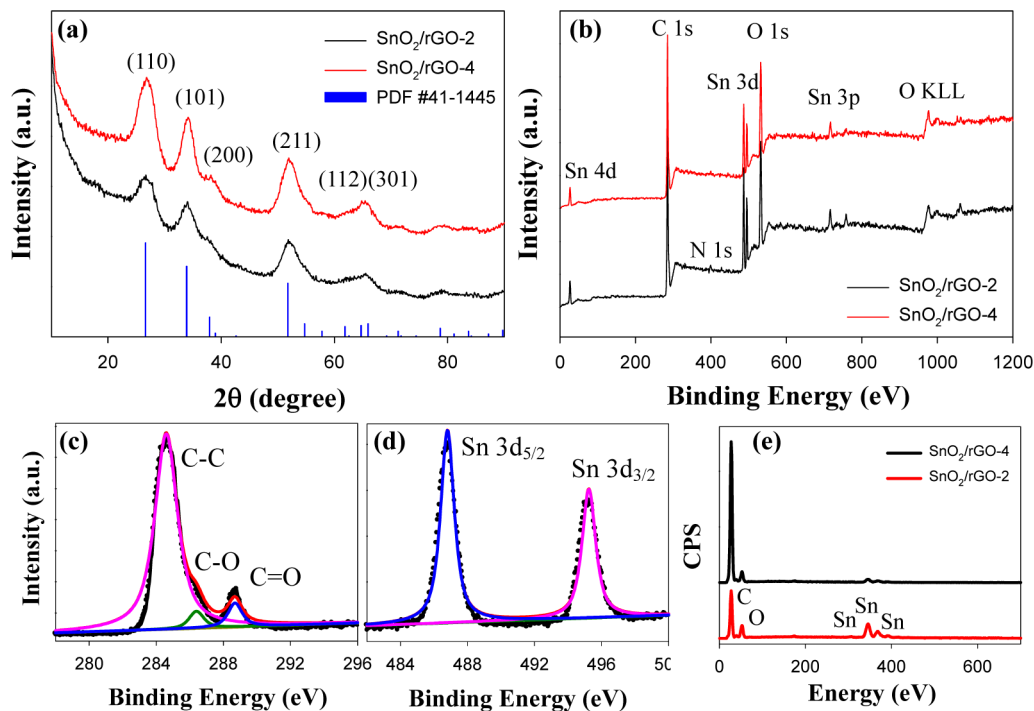

Figure 2. (a) XRD patterns of the 3D SnO_2/rGO hybrids prepared from different Sn precursors. (b) XPS survey spectra of the SnO_2/rGO-2 and SnO_2/rGO-4 samples. High-resolution C 1s (c) and Sn 3d (d) XPS spectra of the SnO_2/rGO-4. (e) EDS spectra of the SnO_2/rGO-2 and SnO_2/rGO-4.
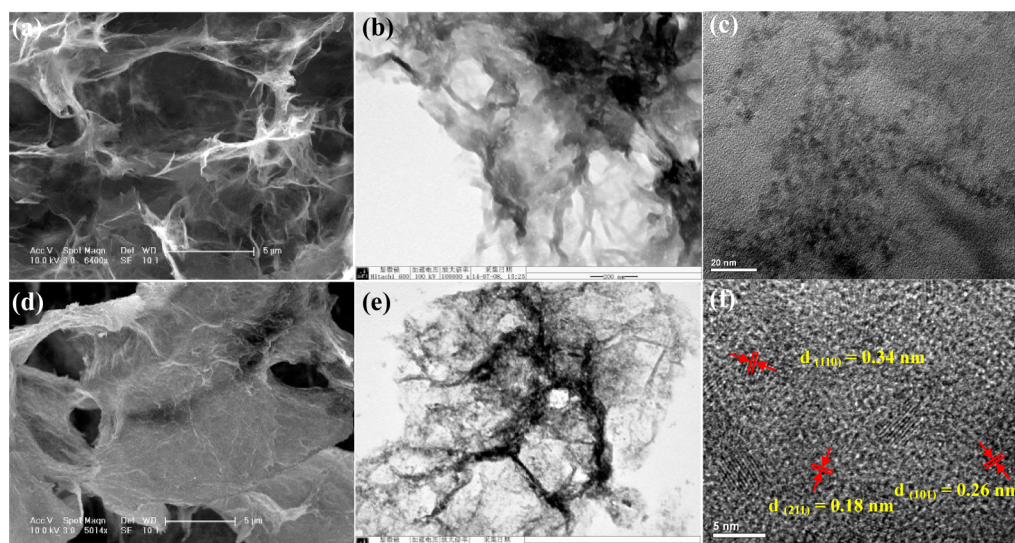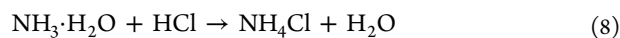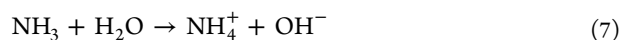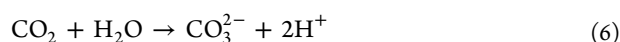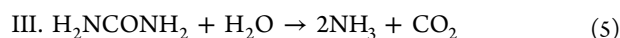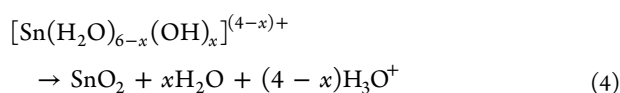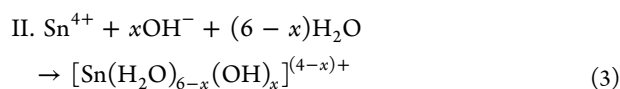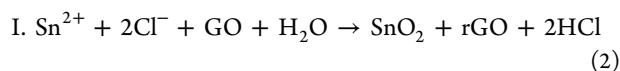
Figure 3. SEM images of the SnO$_2$/rGO-4 (a) and SnO$_2$/rGO-2 (d). TEM images of the SnO$_2$/rGO-4 (b) and SnO$_2$/rGO-2 (e). (c, f) HRTEM images of the SnO$_2$/rGO-4.

acts as a buffering agent. With temperature rising, urea could be decomposed slowly to release NH$_4^+$ and CO$_3^{2-}$, which can promote the nucleation of Sn^{M+} (M = 2, 4) and the formation of nanocrystals. The main reactions from Sn^{2+} and Sn^{4+} could be described as follows:

$$\text{I. } Sn^{2+} + 2Cl^- + GO + H_2O \rightarrow SnO_2 + rGO + 2HCl \tag{2}$$

$$\text{II. } Sn^{4+} + xOH^- + (6-x)H_2O$$
$$\rightarrow [Sn(H_2O)_{6-x}(OH)_x]^{(4-x)+} \tag{3}$$

$$[Sn(H_2O)_{6-x}(OH)_x]^{(4-x)+}$$
$$\rightarrow SnO_2 + xH_2O + (4-x)H_3O^+ \tag{4}$$

$$\text{III. } H_2NCONH_2 + H_2O \rightarrow 2NH_3 + CO_2 \tag{5}$$

$$CO_2 + H_2O \rightarrow CO_3^{2-} + 2H^+ \tag{6}$$

$$NH_3 + H_2O \rightarrow NH_4^+ + OH^- \tag{7}$$

$$NH_3 \cdot H_2O + HCl \rightarrow NH_4Cl + H_2O \tag{8}$$

The crystal structures and compositions of the 3D SnO$_2$/rGO prepared from different Sn precursors were examined by XRD, XPS, and EDS, as shown in Figure 2a−e. It can be seen from Figure 2a that for both SnO$_2$/rGO samples synthesized from Sn^{2+} and Sn^{4+} precursors, their XRD patterns agree well with that of rutile SnO$_2$ (JCPDS card No. 41-1445). Such results suggest that the reactions between acidic GO solutions and Sn^{2+} or Sn^{4+} can both produce rGO-supported SnO$_2$ nanocomposites. By comparing the diffraction peaks of the SnO$_2$/rGO-2 and SnO$_2$/rGO-4, the full-width at half-maximum of the diffraction peaks of SnO$_2$/rGO-4 are larger than that of the SnO$_2$/rGO-2, suggesting the much better crystalline degree and smaller crystal size of SnO$_2$ nanoparticles in the SnO$_2$/rGO-4. By using Scherrer's equation $d = 0.9\lambda/B_{2\theta} \cos\theta$ (λ: wavelength of the X-ray; θ: angle of the peak; $B_{2\theta}$: the peak width at half-height), the average crystalline sizes of the SnO$_2$/rGO-4 and SnO$_2$/rGO-2 were estimated to be about 3 and 7 nm, respectively, which can also be verified by the TEM results.

It is well-known that the morphology and size of nanomaterials are strongly dependent on the synthetic method and formation process. Here, the different formation processes may result in the different particle size of SnO$_2$ nanocrystals in the two samples.

In order to analyze the composition and the chemical states of the SnO$_2$/rGO-4 and SnO$_2$/rGO-2, XPS measurements were carried out. Figure 2b shows the survey spectra of both samples, from which the peaks of C, O, and Sn can be observed. In addition, weak N signals are also present in the survey spectra, which could be from the N-doped graphene introduced by the used urea. From the high-resolution C 1s spectrum of the SnO$_2$/rGO-4 shown in Figure 2c, the three peaks at 284.6, 286.4, and 288.7 eV could be attributed to the C−C, C−O, and C=O bonds in graphene-based composites.[14] Figure 2d shows the Sn 3d spectrum of the SnO$_2$/rGO-4, in which the two strong bands at 486.8 and 495.2 eV and the peak separation of 8.4 eV all indicate the formation of SnO$_2$.[18,20] It should be noted that from the XPS measurements, both samples have high ratio of C to O (>4:1), which can guarantee the high electrical conductivity properties of the formed hybrids. The EDS spectra of the samples shown in Figure 2 e are in a good accord with the results of XPS measurements, with the presence of C, Sn, and O.

The locally magnified SEM, TEM, and HRTEM images of the freeze-dried SnO$_2$/rGO-2 and SnO$_2$/rGO-4 samples are shown in Figure 3a−f. From the SEM images in Figure 3a and d, the 3D aerogel samples exhibit macroporous structure with well-defined interconnected pores at micrometer order. Compared with SnO$_2$/rGO-2, the SnO$_2$/rGO-4 sample appears in a 3D structure with more pores and less layers of graphene nanosheets. For both composites, however, owing to the nanometer-order size, the supported SnO$_2$ nanocrystals can be hardly observed in the SEM images. The TEM images in Figure 3b and e reveal that there are plenty of pores at nanometer order distributing on the 3D graphene sheets, which could be introduced by the lyophilization treatment. The plentiful pores imply that the 3D porous composites possess large surface area which makes them excellent candidates as gas sensing materials. Figure 3c and f present the HRTEM images of the SnO$_2$/rGO-4 composite. From the HRTEM images, well-dispersed SnO$_2$

nanoclusters can be observed clearly, and the average size was measured to be 2−3 nm which is in accordance with the estimated sizes from Scherrer's equation and the previously reported results.[12,13] Also from Figure 3f, the lattice fringes with interplanar spacing of 0.34, 0.26, and 0.18 nm are well resolved, which can be assigned to the (110), (101), and (211) planes of the graphene-supported rutile SnO_2 nanocrystals.

In order to quantitatively determine and compare the specific surface areas and pore volumes of the SnO_2/rGO-2 and SnO_4/rGO-2 composites, multipoint BET surface area and pore volume analyses were carried out based on the nitrogen adsorption−desorption isotherms. The N_2 physisorption isotherms of the two 3D composites and their corresponding Barret−Joyner−Halenda (BJH) pore size distribution curves are shown in Figure 4 a and b. One can see that both samples
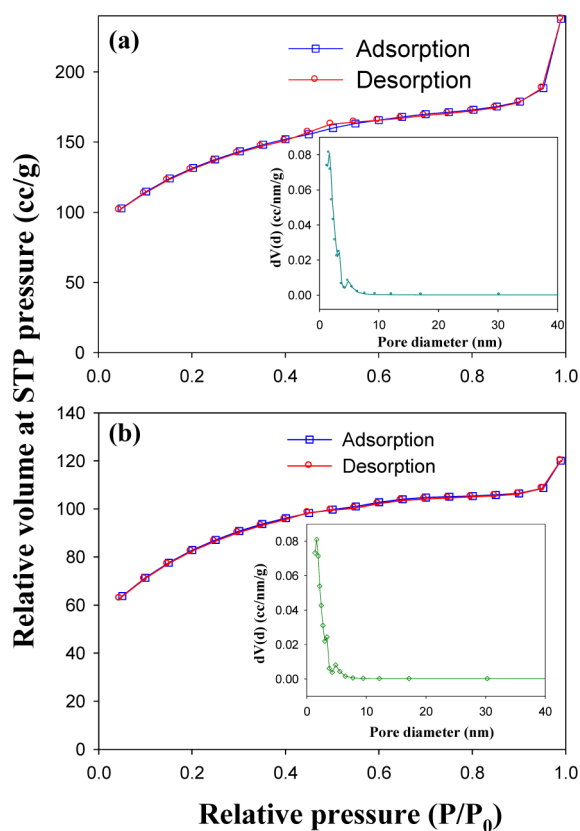

Figure 4. N_2 adsorption−desorption isotherms of the 3D SnO_2/rGO-2 (a) and SnO_2/rGO-4 (b), insets are the corresponding pore size distributions.

exhibit hysteresis loops which resemble the H2 type as per the IUPAC classification. From the measurements, the BET surface areas of SnO_2/rGO-4 and SnO_2/rGO-2 are 441.9 and 281.6 m^2/g, respectively. It should be noted that the BET surface area of the SnO_2/rGO-4 is much higher than those of all the previously reported 3D graphene composites.[14,26] As described above, the high surface area of the present 3D hybrids could be attributed to the plentiful nanopores in the graphene nanosheets. On the basis of BJH model and the desorption data, the average pore radius $dV(d)$ of both samples was calculated to be 1.68 nm, as shown in Figure 4a and b insets. The high surface area and pore volume of SnO_2/rGO-4 can play a significant role in enhancing the electron transport and accelerating the gas diffusion as compared to its counterparts.

Raman spectra of the as-prepared SnO_2/rGO-2, SnO_2/rGO-4, and bare rGO are depicted in Figure 5a. In the spectra of the
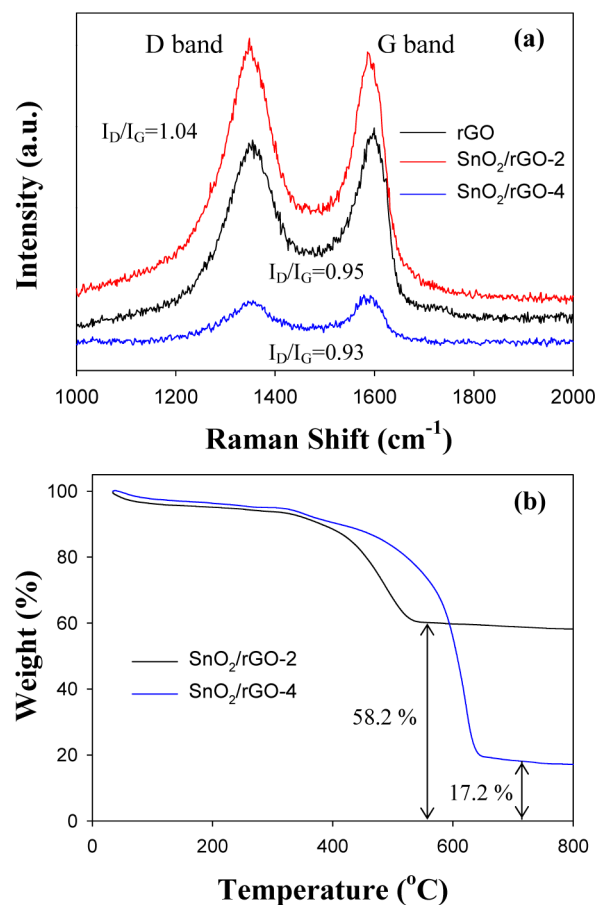

Figure 5. (a) Raman spectra of bare rGO, SnO_2/rGO-2, and SnO_2/rGO-4 composites. (b) TG analysis curves of the 3D SnO_2/rGO hybrids under air atmosphere at a heating rate of 10 °C/min.

three samples, two characteristic peaks at around 1354 and 1599 cm^{-1} are assigned to the D and G bands of graphene, respectively. Compared with bare rGO, the G bands of the SnO_2/rGO-2 and SnO_2/rGO-4 composites exhibit red shifts, which could be attributed to the hole-transporting effect of the SnO_2/rGO hybrids (p-type doping effect).[11] The intensity ratio of D to G band (I_D/I_G) of the SnO_2/rGO-2 (1.04) is higher than that of the bare rGO (0.95), indicating a decrease in the sp^2 carbon domain and a high concentration of defects caused by an increase in vacancies, grain boundaries, amorphous carbon species, and SnO_2 nanoparticles inserted between graphene sheets.[27] However, the I_D/I_G ratio of the SnO_2/rGO-4 (0.93) is very close to that of bare rGO, which is different from other previously reported results. Such result suggests that the average size of the sp^2 domains of the SnO_2/rGO-4 composite was maintained, and thus high conductivity and quickly charge transfer capability could be provided.

Notably, the content of SnO_2 in the composites may directly affect the response of sensors to target gas, so the thermogravimetric analysis was carried to evaluate the mass loading of SnO_2 on the 3D rGO aerogel. Figure 5b depicts the TGA profiles of the SnO_2/rGO-2 and SnO_2/rGO-4 composites as a function of heating temperature from 30 to 800 °C at a rate of 10 °C/min under air conditions. The initial decline of TGA curve below 300 °C corresponds to the mass loss of water and

decomposition of functional groups on the graphene (6.48 wt % for the former and 6.58 wt % for the latter). With temperature increasing, the pyrolysis process of the products shows a sharp drop stage beginning with 350 °C, which is mainly attributed to the decomposition of graphene supporting materials.[10,12] Based on the TGA measurements, approximately 58.2 and 17.2 wt % of SnO_2 were loaded on the SnO_2/rGO-2 and SnO_2/rGO-4 composites, respectively. Compared to the initial weight percentages of $SnCl_4 \cdot 5H_2O$ (74.4%) and $SnCl_2 \cdot 2H_2O$ (64.3%) in the precursors (metal salts and GO), not all the metal salts were converted to SnO_2 composites. On the other hand, the mass loading of nanoparticles on rGO support is mainly dependent on the particle density and particle size deposited on the rGO support. Therefore, the higher loading of SnO_2/rGO-2 may be partially due to the larger size of the SnO_2 nanocrystals in SnO_2/rGO-2 compared to the SnO_2/rGO-4 (as shown in TEM characterizations). The different SnO_2 loadings on the 3D graphene aerogel may directly affect the sensing performances of the gas sensors based on the two composites.[28]

Sensing Properties of the 3D SnO_2/rGO Hybrids for NO_2 Gas Detection. The sensing performances of the gas sensors fabricated from the prepared 3D SnO_2/rGO hybrids were evaluated by their resistance changes upon exposure to NO_2 gas with a controlled concentration at different operation temperatures. To determine the optimal operating temperature, the sensing performance dependent on temperature was studied first. Figure 6a illustrates the responses of the SnO_2/rGO-4 sensor toward 100 ppm of NO_2 at different operating temperatures changing from 22 to 70 °C. It can be seen that the
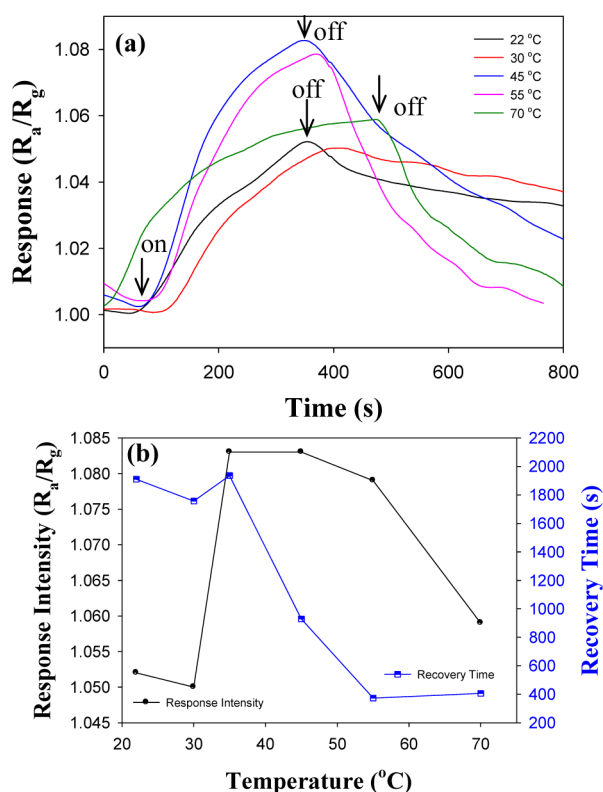
response intensity of the composite increases first with the temperature rising. When the operation temperature was increased to 45 °C, the maximum response value (1.083) was obtained. However, with temperature further increasing, the response intensity appears to have a decline tendency. On the other hand, the recovery time decreases with the operating temperature increasing gradually. The dependence of response intensity and recovery time on operating temperature for NO_2 gas sensing on SnO_2/rGO-4 is shown in Figure 6b. It is clear that the operation temperature is a critical factor to affect the gas sensing performance of the metal oxides/rGO composites. The temperature-dependent gas sensing behavior of SnO_2/rGO-4 is consistent with that reported by Johnson et al.[29] but is totally different from that reported by Zhang and co-workers.[16,20] Theoretically, relative higher temperature can provide more energy to accelerate the transfer of electrons between target gas and sensing materials, including the electrons in the interior of the composites, and overcome the potential barrier between SnO_2 and rGO heterosturcture. From Figure 6b, at 55 °C, the response intensity reaches 1.079 which is a little lower than the best one, but the recovery time is only 373 s which is the shortest one among all the tests. Therefore, taking the response intensity and recovery time into consideration, the optimal working temperature is determined to be 55 °C for the SnO_2/rGO-4. Meanwhile, the optimal operating temperature for SnO_2/rGO-2 was found to be 70 °C.

The sensing performances of the 3D porous SnO_2/rGO-2 and SnO_2/rGO-4 composites were investigated by exposing in different concentrations of NO_2 gas at their optimized operating temperatures (55 and 70 °C). It should be pointed out that these optimum working temperatures are much lower than those reported previously for NO_2 sensing with graphene-supported SnO_2 (~200 °C).[16,30] We also measured the resistances of the studied materials (Supporting Information Figure S1). It can be seen that pure SnO_2 has a very high resistance on the order of 10^8 Ω. However, both SnO_2/rGO-4 and SnO_2/rGO-2 composites exhibit much lowered resistance (on the order of 10^3 Ω). Interestingly, the resistances from the SnO_2/rGO composites are even lower than that of rGO, which could be ascribed to the formed p−n heterojunctions between SnO_2 nanoparticles and rGO. Meanwhile, from the previous studies, due to the excellent conductivity of graphene or other carbon materials, the metal oxide composites supported on carbon materials showed enhanced electronic conductivity compared to the pure metal oxides.[31,32] Therefore, the lowered working temperature from the rGO-supported SnO_2 composites may be partially ascribed to the enhanced electronic conductivity. On the other hand, the formation of p−n junctions between SnO_2 and rGO at the interface makes electron transfer easier, thus lowering the working temperature.[33] The detailed sensing mechanism of the metal oxide/graphene hybrids needs to be further studied. Figure 7a shows the dynamic sensing response of SnO_2/rGO-4 to NO_2 gas with different concentrations (from 14 to 110 ppm) at 55 °C. It can be observed that the response of R_a/R_g increases with the concentration of NO_2 gas increasing. Such concentration-sensitive variation suggests the sensing mechanism of p-type semiconductors (the majority carriers are holes).[15,16] The response of the SnO_2/rGO-4 as a function of NO_2 concentration is plotted in Figure 7d (blue line). It can be seen that, in the whole concentration range, a good linear fit was obtained ($R^2 = 0.993$). From the slope of the calibration line, the sensitivity for NO_2 detection was calculated to be
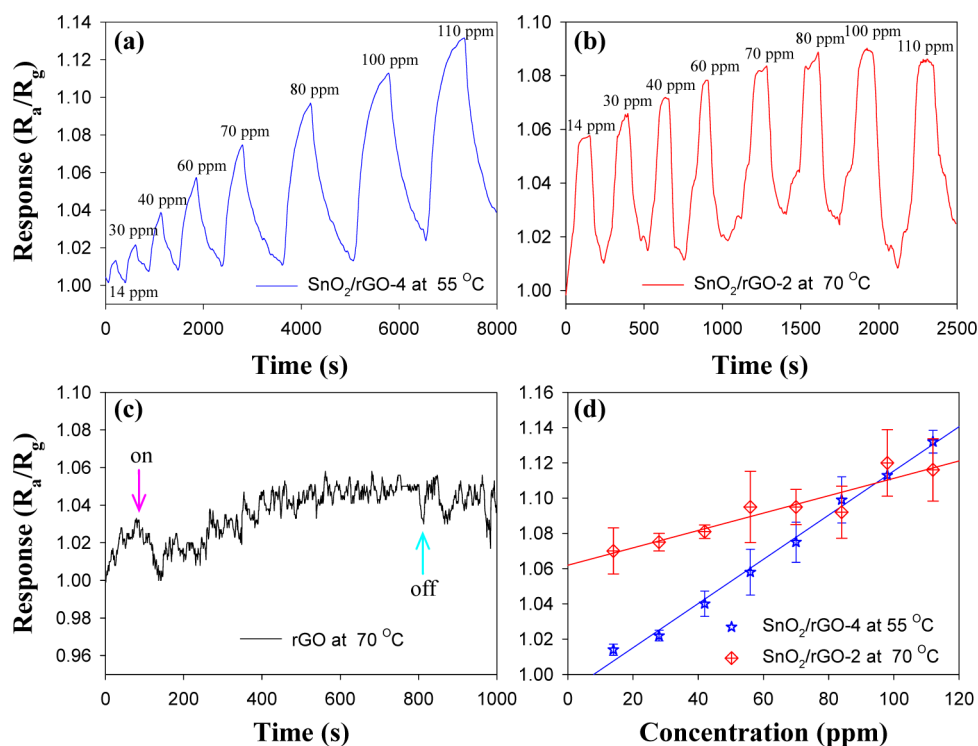

Figure 6. (a) Comparison of the response of gas sensor fabricated from the SnO_2/rGO-4 toward 100 ppm of NO_2 at different operation temperature from 22 to 70 °C. (b) Corresponding response intensity and recovery time as a function of operation temperature to 100 ppm of NO_2.

Figure 7. Dynamic sensing responses of SnO$_2$/rGO-4 (a) and SnO$_2$/rGO-2 (b) sensors upon exposure to NO$_2$ gas with concentrations varying from 14 to 110 ppm. (c) Sensing response of rGO to 100 ppm of NO$_2$ gas at 70 °C. (d) Reponse variations of SnO$_2$/rGO-4 and SnO$_2$/rGO-2 as a function of NO$_2$ concentration. Solid lines show the linear fitting of the experimental data.

0.001 ppm^{-1}. Moreover, the limit of detection (LOD) of the SnO$_2$/rGO-4 was estimated to be 2 ppm based on the LOD = $3S_D/S$ (where S is the slope of linear part of the calibration curve and S_D is the standard deviation of noise in the response curve in air).[34] The wide linear range, high sensitivity, and low detection limit are beneficial for the application of SnO$_2$/rGO-4 in real NO$_2$ gas sensors. The achieved detection limit is comparable to those reported before.[30,35−37] From the sensing response curve shown in Figure 7b, although the SnO$_2$/rGO-2 sensing material shows a little faster response and recovery rate compared to the SnO$_2$/rGO-4, it is not sensitive to the concentration variation of NO$_2$ gas; i.e., low detection sensitivity as shown in Figure 7d (red fitting line) and its sensitivity and LOD were estimated to be 4.9×10^{-4}/ppm and 10.6 ppm, respectively, which are much worse than those of SnO$_2$/rGO-4. Furthermore, in the sensing test, the SnO$_2$/rGO-2 exhibited high noise, which could be induced by the large amount of amorphous carbon species as indicated in the Raman spectrum. For comparison, the sensing property of blank rGO for NO$_2$ gas was also measured. As shown in Figure 7c, almost negligible signal was obtained with the presence of ~100 ppm of NO$_2$ gas, indicating the poor sensing performance of rGO for NO$_2$ gas detection at low temperature. Meanwhile, as shown in Supporting Information Figure S2, the sensing performance of pure SnO$_2$ for NO$_2$ gas is much poorer, and higher operating temperature is needed compared to the graphene-supported SnO$_2$ composites.

The sensing selectivity of SnO$_2$/rGO-4 was also studied upon exposure to various gases and vapors, including NO$_2$, CO, ethanol, ethylene glycol, phenylcarbinol, acetone, toluene, ammonia, trihalomethanes (THMS), and formaldehyde. As shown in Figure 8, among the studied analytes, the sensor shows the strongest response toward NO$_2$, demonstrating the
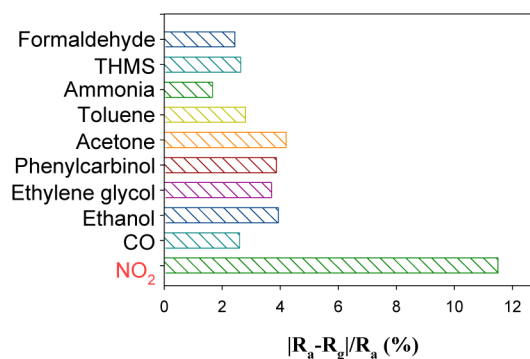

Figure 8. Detection selectivity of SnO$_2$/rGO-4 upon exposure to various vapors (~110 ppm) operating at 55 °C.

high sensing selectivity of SnO$_2$/rGO-4 for NO$_2$ detection. A gas can be detected by a sensor only when it can react with anion oxygen on the surface of semiconductor composite at a certain temperature. The adsorption abilities and activities of different target gases are different at a given temperature, which may lead to the detection selectivity of semiconductor-based sensors. On the other hand, as mentioned above, oxygen vacancies and antisite defects can act as channel entrances for the gas molecules and can effectively control the diffusion of small molecular gases. Therefore, it is difficult for large gas molecules to enter and diffuse in the 3D porous composite, resulting in less chance to react with the anion oxygen in the composite and leading to a sensing selectivity for particular gas molecules. More studies on sensing selectivity of graphene-supported composites are currently underway, and deep understanding of the selectivity is still needed.

CONCLUSION

In conclusion, we have experimentally demonstrated the fabrication of 3D mesoporous SnO_2/rGO composites using different tin precursors and their application as sensing materials for NO_2 gas detection. The structural characterizations showed that the 3D composites prepared from Sn^{4+} precursor have plentiful nanopores in the aerogel structure and thus exhibited extremely large surface area. Due to the porous structure, good electrical conductivity and enhanced surface/interface adsorption sites, the as-synthesized SnO_2/rGO hybrid is a promising sensing material for gas detection. The sensing performances of the SnO_2/rGO materials were evaluated for NO_2 gas detection. It was found that the sample prepared from Sn^{4+} (SnO_2/rGO-4) showed much higher sensing performance than that of the hybrid material obtained with Sn^{2+} precursor (SnO_2/rGO-2). At the optimal operating temperature (55 °C), the SnO_2/rGO-4 demonstrated high sensitivity (0.001 ppm^{-1}), low detection limit (2 ppm), and a wide linear range. The excellent sensing properties render the 3D SnO_2/rGO hybrid material potential application in real gas sensors. Also the present study opens up a possibility of using highly porous 3D graphene aerogel-supported metal oxide nanocrystals as sensing platform for practical gas detection.

ASSOCIATED CONTENT

Ⓢ Supporting Information

Comparison of the resistances of the studied materials and the sensing response of pure SnO_2 to NO_2 gas. This material is available free of charge via the Internet at http://pubs.acs.org.

AUTHOR INFORMATION

Corresponding Author

*E-mail: weichen@ciac.ac.cn.

Notes

The authors declare no competing financial interest.

ACKNOWLEDGMENTS

REFERENCES

(1) Zhou, X.; Fu, W.; Yang, H.; Zhang, Y.; Li, M.; Li, Y. *Mater. Lett.* **2013**, *90*, 53−55.

(2) Zhang, J.; Guo, J.; Xu, H.; Cao, B. *ACS Appl. Mater. Interfaces* **2013**, *5*, 7893−7898.

(3) Wang, L.; Chen, Y.; Ma, J.; Chen, L.; Xu, Z.; Wang, T. *Sci. Rep.* **2013**, *3*, 3500.

(4) Gu, C.; Xu, X.; Huang, J.; Wang, W.; Sun, Y.; Liu, J. *Sens. Actuators, B* **2012**, *174*, 31−38.

(5) Schedin, F.; Geim, A. K.; Morozov, S. V.; Hill, E. W.; Blake, P.; Katsnelson, M. I.; Novoselov, K. S. *Nat. Mater.* **2007**, *6*, 652−655.

(6) Fowler, J. D.; Allen, M. J.; Tung, V. C.; Yang, Y.; Kaner, R. B.; Weiller, B. H. *ACS Nano* **2009**, *3*, 301−306.

(7) Zhou, L.; Shen, F.; Tian, X.; Wang, D.; Zhang, T.; Chen, W. *Nanoscale* **2013**, *5*, 1564−1569.

(8) Singh, G.; Choudhary, A.; Haranath, D.; Joshi, A. G.; Singh, N.; Singh, S.; Pasricha, R. *Carbon* **2012**, *50*, 385−394.

(9) Huang, Q.; Zeng, D.; Li, H.; Xie, C. *Nanoscale* **2012**, *4*, 5651−5658.

(10) Guo, Q.; Zheng, Z.; Gao, H.; Ma, J.; Qin, X. *J. Power Sources* **2013**, *240*, 149−154.

(11) Xu, C. H.; Sun, J.; Gao, L. *J. Mater. Chem.* **2012**, *22*, 975−979.

(12) Wang, B.; Su, D.; Park, J.; Ahn, H.; Wang, G. *Nanoscale Res. Lett.* **2012**, *7*, 215.

(13) Zhang, L. S.; Jiang, L. Y.; Yan, H. J.; Wang, W. D.; Wang, W.; Song, W. G.; Guo, Y. G.; Wan, L. J. *J. Mater. Chem.* **2010**, *20*, 5462−5467.

(14) Dutta, D.; Chandra, S.; Swain, A. K.; Bahadur, D. *Anal. Chem.* **2014**, *86*, 5914−5921.

(15) Neri, G.; Leonardi, S. G.; Latino, M.; Donato, N.; Baek, S.; Conte, D. E.; Russo, P. A.; Pinna, N. *Sens. Actuators, B* **2013**, *179*, 61−68.

(16) Marichy, C.; Russo, P. A.; Latino, M.; Tessonnier, J. P.; Willinger, M. G.; Donato, N.; Neri, G.; Pinna, N. *J. Phys. Chem. C* **2013**, *117*, 19729−19739.

(17) Chang, Y.; Yao, Y.; Wang, B.; Luo, H.; Li, T.; Zhi, L. *J. Mater. Sci. Technol.* **2013**, *29*, 157−160.

(18) Meng, F. L.; Li, H. H.; Kong, L. T.; Liu, J. Y.; Jin, Z.; Li, W.; Jia, Y.; Liu, J. H.; Huang, X. J. *Anal. Chim. Acta* **2012**, *736*, 100−107.

(19) Lin, Q. Q.; Li, Y.; Yang, M. *J. Sens. Actuators, B* **2012**, *173*, 139−147.

(20) Zhang, H.; Feng, J.; Fei, T.; Liu, S.; Zhang, T. *Sens. Actuators, B* **2014**, *190*, 472−478.

(21) Yin, L.; Chen, D. L.; Cui, X.; Ge, L. F.; Yang, J.; Yu, L. L.; Zhang, B.; Zhang, R.; Shao, G. S. *Nanoscale* **2014**, *6*, 13690−13700.

(22) Russo, P. A.; Donato, N.; Leonardi, S. G.; Baek, S.; Conte, D. E.; Neri, G.; Pinna, N. *Angew. Chem., Int. Ed.* **2012**, *51*, 11053−11057.

(23) Song, H. J.; Zhang, L. C.; He, C. L.; Qu, Y.; Tian, Y. F.; Lv, Y. *J. Mater. Chem.* **2011**, *21*, 5972−5977.

(24) Jensen, K. M.; Christensen, M.; Juhas, P.; Tyrsted, C.; Bojesen, E. D.; Lock, N.; Billinge, S. J.; Iversen, B. B. *J. Am. Chem. Soc.* **2012**, *134*, 6785−6792.

(25) Wang, H.; Rogach, A. L. *Chem. Mater.* **2014**, *26*, 123−133.

(26) Wang, R.; Xu, C.; Sun, J.; Gao, L.; Yao, H. *ACS Appl. Mater. Interfaces* **2014**, *6*, 3427−3436.

(27) Chen, C.; Wang, L.; Liu, Y.; Chen, Z.; Pan, D.; Li, Z.; Jiao, Z.; Hu, P.; Shek, C. H.; Wu, C. M.; Lai, J. K.; Wu, M. *Langmuir* **2013**, *29*, 4111−4118.

(28) Li, L.; Liu, M. M.; He, S. J.; Chen, W. *Anal. Chem.* **2014**, *86*, 7996−8002.

(29) Johnson, J. L.; Behnam, A.; Pearton, S. J.; Ural, A. *Adv. Mater.* **2010**, *22*, 4877−4880.

(30) Neri, G.; Leonardi, S. G.; Latino, M.; Donato, N.; Baek, S.; Conte, D. E.; Russo, P. A.; Pinna, N. *Sens. Actuators, B* **2013**, *179*, 61−68.

(31) Liu, M. M.; He, S. J.; Chen, W. *Nanoscale* **2014**, *6*, 11769−11776.

(32) He, S. J.; Zhang, B. Y.; Liu, M. M.; Chen, W. *RSC Adv.* **2014**, *4*, 49315−49323.

(33) Mashock, M.; Yu, K. H.; Cui, S. M.; Mao, S.; Lu, G. H.; Chen, J. H. *ACS Appl. Mater. Interfaces* **2012**, *4*, 4192−4199.

(34) Paul, R. K.; Badhulika, S.; Saucedo, N. M.; Mulchandani, A. *Anal. Chem.* **2012**, *84*, 8171−8178.

(35) Zhang, H.; Feng, J. C.; Fei, T.; Liu, S.; Zhang, T. *Sens. Actuators, B.* **2014**, *190*, 472−478.

(36) Mao, S.; Cui, S. M.; Lu, G. H.; Yu, K. H.; Wen, Z. H.; Chen, J. H. *J. Mater. Chem.* **2012**, *22*, 11009−11013.

(37) Cui, S. M.; Wen, Z. H.; Mattson, E. C.; Mao, S.; Chang, J. B.; Weinert, M.; Hirschmugl, C. J.; Gajdardziska-Josifovska, M.; Chen, J. H. *J. Mater. Chem. A* **2013**, *1*, 4462−4467.